mics and Kinetic Constants for the Diborane-Borane Equilibrium," *Journal of the American Chemical Society*, Vol. 75, 1953, pp. 1003–1004.

[5] Bragg, J. K., McCarty, L. V., and Norton, F. J., "Kinetics of Pyrolysis of Diborane," *Journal of the American Chemical Society*, Vol. 73, 1951, pp. 2134–2140.

[6] Clarke, R. P. and Pease, R. N., "A Preliminary Study of the Kinetics of Pyrolysis of Diborane," *Journal of the American Chemical Society*, Vol. 73, 1951, p. 2132.

[7] Clapper, T. W., "Final Report for High-Energy Fuels Project. Vol. II: Theory of Diborane Pyrolysis," Vol. II, TR NR AST-TDR-62-1025, June 1962, AFN, Inc., Los Angeles, Calif.

[8] Roth, W. and Bauer, W. H., "Combustion of Diborane-Oxygen Mixtures at the Second Explosion Limit," *Fifth Symposium on Combustion*, Reinhold, New York, 1955, pp. 710–717.

[9] Goldstein, M. S., "Oxidation of Diborane," Ph.D. thesis, 1961, Rensselaer Polytechnic Institute, Troy, N.Y.

[10] Adams, R. M., ed., *Boron, Metallo-Boron Compounds and Boranes*, Interscience Publishers, New York, 1964.

[11] Weiss, H. G. and Shapiro, I., "Mechanism of the Hydrolysis of Diborane in the Vapor Phase," *Journal of the American Chemical Society*, Vol. 75, 1953, pp. 1221–1224.

[12] Rhein, R. A., "Processing Spectrophotometric Measurements To Compute Chemical Reaction Rates and Correlate Them to a Rate Equation: A Computer Program," TR 32-1384, April 15, 1969, Jet Propulsion Lab., Pasadena, Calif.

MARCH 1971 AIAA JOURNAL VOL. 9, NO. 3

Behavior of a Large Nonequilibrium MHD Generator

REINER DECHER*
University of Washington, Seattle, Wash.

AND

MYRON A. HOFFMAN†
University of California, Davis, Calif.

AND

JACK L. KERREBROCK‡
Massachusetts Institute of Technology, Cambridge, Mass.

A large nonequilibrium MHD generator of the linear, segmented-electrode, Faraday type has been studied both experimentally and theoretically. Experiments have been run at the following nominal operating conditions: generator Mach number of 2.2 with a mass flow of 0.4 kg/sec^{-1} of helium seeded with about 0.3% cesium; stagnation conditions were 2000°K and about 5-atm pressure. The loaded generator exhibited several unusual features, including a very slow increase in the load currents axially and very large anode drops. The Hall voltage was a small fraction of its ideal value. At short circuit, load currents at least five times those possible with frozen ionization were drawn; but these currents were still far below those predicted by one-dimensional theory. At open circuit the transverse voltages were usually very low near the inlet and exit but as large as 0.6 of the ideal value near the channel center; negative electrode drops were measured on both cathodes and anodes. A theoretical model is proposed to explain this behavior. It is hypothesized that highly conducting layers exist along the electrode walls which short the generator through the end regions at open circuit. These layers exist because the transverse current is impeded at the insulator segments of the electrode wall, leading to a larger conductivity there than in the main flow. Under load these layers interact with a two-dimensional inlet relaxation front to couple the generator end-to-end, producing the very slow axial build-up of the load current. The proposed model is shown to explain the major features of the experimental results.

1. Introduction

THE work to be reported here is part of a continuing study of the behavior of nonequilibrium MHD generators. The generator to be discussed is of the segmented Faraday type.[1–3] Its mass flow of 0.4 kg^{-1} is large enough to prevent viscous effects from being dominant, whereas the supersonic flow and large Hall parameter ideally should result in electron temperatures well above the gas stagnation temperature with reasonable load factors.

The aims of the present investigation were mainly two. The first was to improve on the preionization. The second was to provide more detailed instrumentation than the earlier experiments, in order to more clearly delineate the current pattern in the generator. The first objective has been achieved, in part, by establishing the preionizing discharge outside of the magnetic field, ahead of the nozzle throat; and, as we shall see, this has resulted in the generator's producing large load currents near short circuit.

With the information derived from the more detailed instrumentation, it has been possible to construct a simple model which explains the behavior of the generator both at open circuit and under load in terms of shorting by end loops which are coupled to the channel center and to the loads by highly conducting layers along the electrode walls.

Received November 7, 1969; revision received June 3, 1970. This research was supported by the Aero Propulsion Laboratory, Aerospace Power Division, USAF, under Contract AF33(615)-67-C-1148 with the Research Laboratory of Electronics, M.I.T.

* Assistant Professor, Department of Aeronautics and Astronautics.

† Professor, Department of Mechanical Engineering. Associate Fellow AIAA.

‡ Professor, Department of Aeronautics and Astronautics. Associate Fellow AIAA.

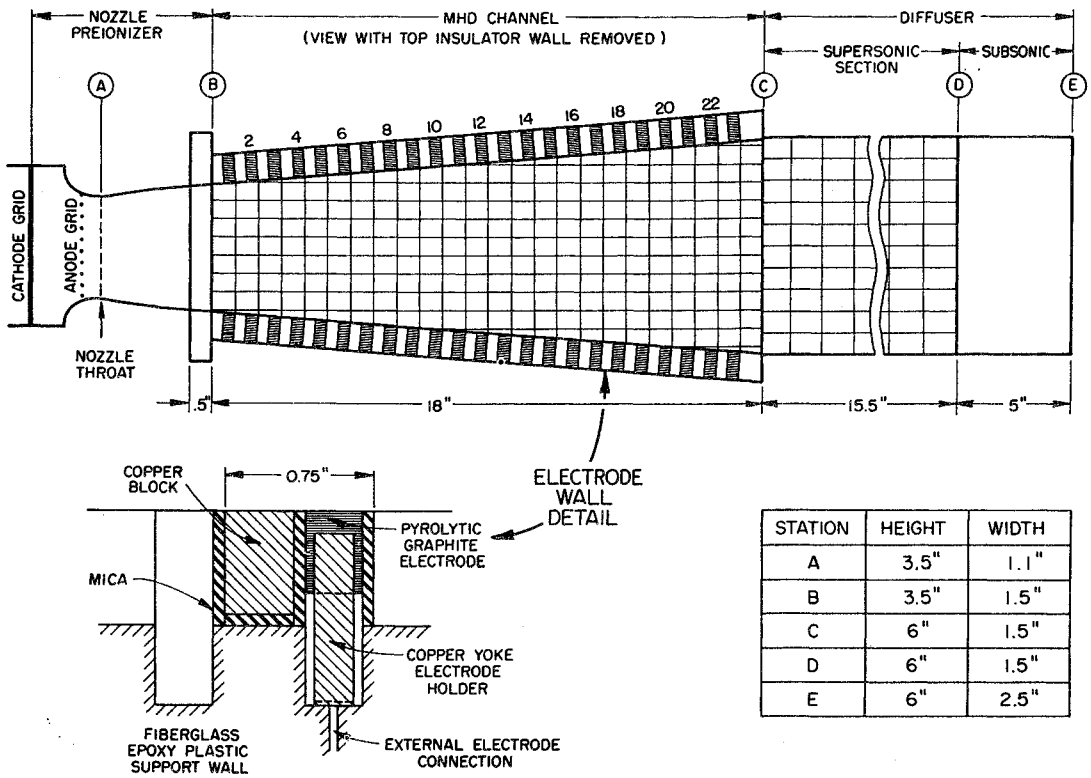

STATION	HEIGHT	WIDTH
A	3.5"	1.1"
B	3.5"	1.5"
C	6"	1.5"
D	6"	1.5"
E	6"	2.5"

Fig. 1 Schematic of the channel, showing nozzle, active section and diffuser with electrode detail.

2. Apparatus and Instrumentation

Table 1 summarizes the design parameters of the generator. The flow channel, shown schematically in Fig. 1, consists of a nozzle, which incorporates the preionizer grids; the active generator section; and the diffuser. A more detailed description than will be given here is available in Ref. 2.

2.1 Nozzle—Preionizer

The nozzle was a water-cooled copper design. The location of the preionizer ahead of the nozzle throat permitted its electrodes, in the form of wire grids, to be in the flow where they would be heated and produce a fairly uniform discharge. The drag associated with the grids in the subsonic flow is tolerable. There are, however, disadvantages to this location. Electron-ion recombination is accelerated in the high pressure region, and there is a time lag of about 100 μsec until the plasma is convected into the generator. To reduce the recombination, the supersonic length of the nozzle was minimized by expanding the flow in two directions.

2.2 Electrode Walls

The Faraday geometry requires a large number of electrodes, each with an independent load circuit. The analysis of Kerrebrock[4] was used to determine the optimal pitching distance and electrode width for eliminating the electrode-shorting instability. The ratio of insulator width to electrode width in the final design was about 0.7. The theory suggested that rather coarse segmentation ratios (5–10) are best for minimizing the effects of current concentrations and the resultant nonuniform Joule heating. An electrode pitch of 0.75 in. was selected so that a segmentation ratio of 4.7 at the inlet to 8.0 at the exit resulted. The theory also suggests that the shorting instability on the electrode wall can be suppressed by lowering the mean plasma temperatures near the wall, but unfortunately the electrodes require high temperatures for emission. The compromise selected consisted in making the electrodes of pyrolytic graphite, with the plane of stratification parallel to the gas flow direction, alternated with cold copper insulator segments surrounded by mica. The aerodynamic heat transfer should have been sufficient to heat the electrode surface to a temperature near the adiabatic wall temperature in less than 1 sec, in the absence of the cool copper segments. To minimize the ohmic loss associated with the relatively high electrical resistivity of the pyrolytic graphite normal to the electrode surface, electrical contact was made with the graphite about $\frac{1}{8}$ in. from the surface, by means of a copper C-clamp attached as shown in Fig. 1. The estimated resistance per load pair due to electrode internal resistance was then less than 1 Ω.

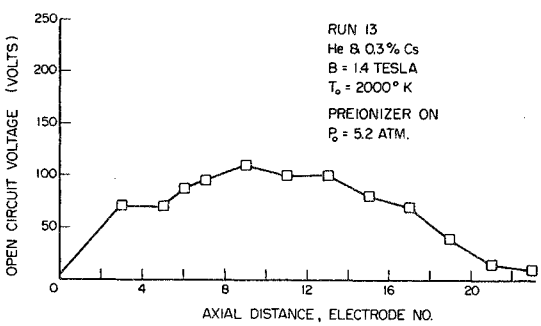

Fig. 2 Open circuit voltage distribution for run 13.

Table 1 Generator design parameters

Working fluid	He + 0.0023 Cesium
Mass flow rate	0.4 kg/sec^{-1}
Stagnation temperature	2000°K
Stagnation pressure	5 atm
Thermal power	4.2 megawatts
Mach number	2.2
Static pressure in generator	0.3–0.6 atm
Magnetic field	1.4 Tesla
Hall parameter	2–8
Induced electric field	50 v/cm

Table 2 Summary of experimental conditions and principal observation

Run	Stagnation pressure, atm	Hall parameter (frozen)	Load resistance, Ω	Seed fraction	Preionizer power, kw	Principal result
10	4.5	6.3	3	0.0023	20 (Arc)	Stagnation pressure rise with B turned off
13	5.1	4.4	o.c.	0.0012	6	End-loop shorting
13	4.3	5.1	10	0.0023	26 (arc?)	Large load current and Hall voltage
13	3.9	5.1	3	0.0023	33 (arc?)	
13	3.7	5.1	s.c.	0.0023	30 (arc?)	
15	4.8	5.1	s.c.	0.0023	0	Most complete pressure data
16			s.c.	0.0023	7	Electron temperature at inlet

2.3 Insulator Walls

The insulator walls or top and bottom of the channel are made of magnetically soft iron blocks $\frac{7}{8}$ in. deep. These blocks are electrically insulated from each other by $\frac{1}{16}$ in. of mica in the transverse and axial directions. The pitching distances are $\frac{1}{2}$ and $\frac{3}{4}$ in., respectively. These blocks are sufficiently deep to make their temperature rise during the experiment negligible. In addition, they form a low magnetic reluctance path, raising the magnetic field strength in the channel by about 15%.

2.4 Diffuser

Since the pressure in the generator was below atmospheric, a diffuser was required to discharge to the atmosphere. It consists of a rectangular channel of constant cross section in which weak shocks interact with the thickening boundary layers on the walls to reduce the Mach number to unity. A diverging section slows the flow further. Because the diffuser inlet is at the Hall potential it was constructed of insulated copper blocks on a fiberglass backing, in the same fashion as the insulator walls. Fig. 1 shows the block pattern.

2.5 Instrumentation

The block-construction of the insulator walls permitted detailed measurements of the potential distribution in the generator. Block to block transverse voltages were measured at electrode numbers 6 and 19, and centerline Hall voltages were measured from 2–6, 6–12, 12–17, and 17–23. Hall voltages were also measured at the same axial stations along the cathode wall. In addition to these voltage measurements, the usual load currents and voltages were measured on 11 of the 23 load circuits.

The gasdynamic behavior of the generator was determined through measurement of stagnation pressures at the channel inlet (which is the heater pressure) and at the exit. The latter measurement was obtained by means of a water-cooled pitot probe located at the end of the generator's active section. Static pressures were measured axially along the centerline as well as at points away from the centerline to obtain transverse pressure distributions.

Electron density and temperature measurements at the channel inlet were also attempted in this series of experiments. The 6P continuum radiation of the cesium plasma was monitored with photomultipliers at two wavelengths. The details of the experimental technique are described in Ref. 2.

The individual load circuits to which the 23 electrodes are connected consists of 6 resistive loads, including open circuit; 100 Ω, 25 Ω, 10 Ω, 3 Ω, and short circuit which were sequentially selected during the run to permit the tracing of a voltage-current characteristic.

3. Experimental Results

A number of experimental runs were conducted, each with slightly different conditions. The results to be presented here are necessarily a synthesis of the complete set. Table 2 lists the major parameters of the experiments which will be cited, along with the principal results derived from them. In this table, the Hall parameter is the microscopic value evaluated at the channel center (static pressure at station 13) assuming that the electron temperature is frozen at stagnation conditions.

3.1 Gas Dynamic Data

The static pressure measurements confirmed that the flow Mach number at the generator inlet was about 2.2 and that the flow in the generator was supersonic with perhaps weak shocks near the inlet and exit. The static pressure did not vary much with load condition except at short circuit, when a sharp pressure rise occurred near the exit. This rise is probably due in part to lower inlet stagnation pressure and in part to an increased MHD interaction.

The electromagnetic forces in the plasma influenced the stagnation pressure drop appreciably. When the magnetic field was turned off during one run, the stagnation pressure at the generator exit rose almost 15 psi. This degree of interaction implies a conductivity of about 50 mho/m which, as we shall see, is consistent with values obtained from the magnitude of the load currents. These points are discussed further in Ref. 3.

3.2 Electrical Data

As is evident from Table 2, the most complete set of electrical data was obtained in run 13. Figure 2 shows the open circuit voltage distribution for this run. It exhibits a maximum near the channel center with a small voltage at the exit. The magnitude of the open circuit voltage is significantly less than its ideal value of some 600 v near the channel center. The same general distribution has been found in several runs. In some previous runs, reported in Ref. 1, larger open circuit voltages were obtained, but the distribution along the channel was similar. Hall voltage distributions along the cathode wall are shown in Fig. 3.

The magnitude of the Hall field is much smaller than the ideal value for the loaded conditions. It is nearly independent of the load current, over a range of load current densities from 0.1 to 4 amp/cm^{-2}. At open circuit, the Hall field is smaller than for the loaded conditions and much smaller than the theoretical value due to channel divergence.

Transverse open circuit voltage profiles at stations 6 and 19 are given in Fig. 4 for run 13. The most striking feature of these data is the "reversed voltage drops" at both cathode and anode near the inlet, and at the anode near the channel

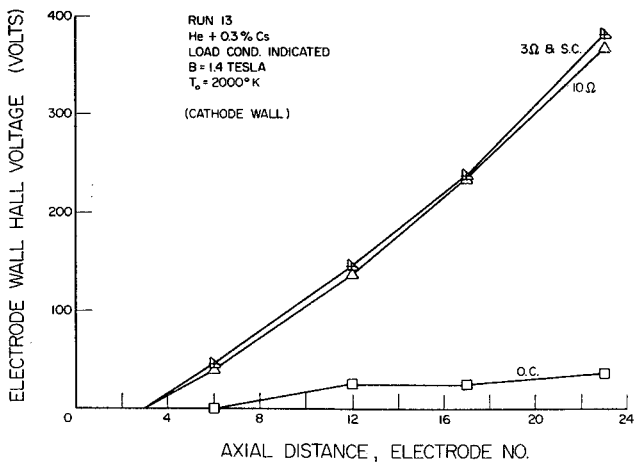

Fig. 3 Axial voltage distribution for run 13.

exit at open circuit. As we shall see, this behavior is indicative of current layers along the electrode walls.

When load currents were drawn, the anode voltage drop reverted to normal polarity, as did the cathode drop near the inlet. However, the magnitude of the anode drops cannot be explained by emission phenomena alone. It is probably due to flow separation from the anode wall.

The load current distribution is shown for various load resistances in Fig. 5. We note an increasing current with decreasing load resistance, as expected, and a rather unexpected variation of load current along the channel. This variation of load current along the channel will be explained below.

The magnitude of the short circuit current density at its maximum is much larger than the current density expected from an electron mole fraction frozen at stagnation conditions indicating that some magnetically induced nonequilibrium ionization has been achieved.

The magnitude of the load currents are correlated to the performance of the preionizer. Generally it was observed that, when the preionizer drew current, current flow to the loads also occurred.

4. Model for the Generator

The model which we propose to explain this rather complex behavior is shown schematically in Fig. 6. Its principal features are: 1) a core region, in which the current flow is governed by the bulk properties of the plasma and by electric fields imposed by the bounding regions; for most operating conditions, the axial field (E_x) is small compared to the ideal Hall field, so that the current has a large Hall (j_x) component. Furthermore, for most operating conditions so far attained, the transverse field (E_y) is small compared to UB, so that the core is nearly shorted transversely also. As a result of these two conditions, the current pattern in the core flow is nearly independent of the electrical boundary conditions. That is, it acts as a fixed current source; 2) highly conducting layers along the electrode walls; these layers exist because the transverse current is impeded at these walls[4,5] on the insulating segments, and at all points at open circuit. Thus, the effective conductivity along the wall is approximately the scalar value, with the result that even a small Hall field (E_x) can drive large currents in these layers. Because their impedance is so low, the layers can redistribute the current which they collect from the core flow in complex ways.

The anode and cathode layers will be modeled by a region of fixed height d having a conductivity, σ_A or σ_C, which depends on the axial current in the layer. That this model represents an oversimplification will become clear later. Nevertheless, it does seem to represent the major features of the actual layers and is simple enough to be readily analyzed; and 3) end regions, just upstream and downstream of the magnetic field region; they are especially important in this type of generator for two reasons. First, since the Hall field is small, the effective conductivity of the plasma in the generator region is reduced roughly by the factor $1/(1 + \beta^2)$, relative to that in the end regions. Secondly, the end regions are coupled to the core flow by the electrode wall layers. These effects combine to make the end shorts extremely damaging, particularly at open circuit.

An examination of the equations which govern the current flow and the electric fields in the generator reveals that the relaxation of the electron density from the nozzle exit value to the higher value supported by the Joule dissipation in the generator is intrinsically two-dimensional.[6] This relaxation occurs along a front which lies at an angle to the flow (Fig. 6). The current flow vector makes an angle with the y axis which is $\tan^{-1}t$, where $t = (\beta - \beta_{app})/(1 + \beta\beta_{app})$ and β_{app} is defined by E_x/E_y'. From the kinetics of the process one can show that the relaxation region is a fraction of a centimeter in thickness which is small compared to the characteristic dimensions of the generator. One can therefore think of this region as an ionization front. The conductivity and hence the current will rise across the front. We will denote by r the ratio of the current density behind the front to the current density ahead of the front.

It must be noted that we have assumed that a steady solution exists. This may not be the case. The relaxation may, in fact, be basically unsteady, occurring by the formation of convected electrothermal (or ionization) instabilities. In that case the present analysis would be qualitatively wrong. We advance the steady mode because it appears to offer an explanation of some aspects of the generator's behavior.

We note first from Fig. 4 that there is an abrupt change in the transverse field near the centerline of the channel at station 6. This is where the proposed front would cross the axis, since $\beta \simeq 5$ and $\beta_{app} \simeq 0.2$, giving $t = 2.4$. This behavior has been observed in several sets of data. Further, there is, as we shall see below, a tendency for the load current to peak toward the exit end of the channel, even at short circuit. This tendency may be connected with the relaxation process since it causes smaller currents to flow into the cathode layer near the inlet.

4.1 Simplified Equations

Referring to Fig. 6, and using the model previously proposed, Ohm's law for an assumed uniform core region becomes

$$j_y(x,h) = r\sigma^*UB(K - 1) \doteq -j^* \qquad (1)$$

$$j_y(x,-h) = nr\sigma^*UB(K - 1) \doteq -nj^*$$

where

$$n = 1/r \text{ for } x < 2\text{th}$$

$$n = 1 \text{ for } x > 2\text{th}$$

and σ^* is an effective conductivity given by

$$\sigma^* = (1 + \beta_{app}\beta)/(1 + \beta^2)\ \sigma \qquad (2)$$

These currents flow into the electrode wall layers, which in turn couple to the loads and to the end regions. To analyze this coupling, we must compute the current flow through the layers and loads, taking account of the voltages produced by the current flow in them. As previously stated, it will be assumed that these voltages are so small that they do not appreciably influence $j_y(x,h)$ and $j_y(x,-h)$, except that an average $K(x)$ and β_{app} will be retained in Eqs. (1)

From curl $\bar{E} = 0$ which is the condition for the existence of a potential, we find that

$$V_L(x) - V_L(0) = \int_0^x (E_{xC} - E_{xA})dx \qquad (3)$$

where E_{xC} and E_{xA} are the fields along the cathode and anode walls, and $V_L(x)$ is the load voltage.

From div $\bar{j} = 0$ the average axial current densities in the layers are related to the core currents by,

$$d(dj_{xA}/dx) = j_y(x,h) - j_L(x) = -j^* - j_L \qquad (4)$$

$$d(dj_{xC}/dx) = -j_y(x,-h) + j_L(x) = nj^* + j_L \qquad (5)$$

where j_L is the effective load current density. The electric fields in the layers will be taken as

$$E_{xC} = j_{xC}/\sigma_C + \beta j_L/\sigma_C \qquad E'_{yC} = j_L/\sigma_C - \beta j_{xC}/\sigma_C \qquad (6a)$$

$$E_{xA} = j_{xA}/\sigma_A + \beta j_L/\sigma_A \qquad E'_{yA} = j_L/\sigma_A - \beta j_{xA}/\sigma_A \qquad (6b)$$

Note that the transverse component of current in the layer has been taken to be j_L. The layers exist, in fact, because $j_L \neq j_y$, so that this approximation gives the correct qualitative behavior, although some average of j_L and j_y may be more nearly correct. Now $V_L(x) = \rho j_L$, where ρ is a resistivity (Ω cm^2) for the loads, so that Eq. (3) may be written

$$d/dx\,(\rho j_L) = E_{xC} - E_{xA} = (j_{xC}/\sigma_C - j_{xA}/\sigma_A) + \beta j_L(1/\sigma_C - 1/\sigma_A) \qquad (7)$$

The essential physical content of Eq. (7) is that the rate of change of the load voltage in x is limited by the electric fields along the electrode walls. An abrupt change of ρj_L would require a large value of either E_{xC} or E_{xA}, which the layers cannot support. Thus, for ρ constant in x, the rate of rise of j_L is limited by these layers. As ρ increases, dj_L/dx must decrease. As we shall see, this effect explains the slow "inlet relaxation" (i.e., slow load current and voltage build-up) observed in the experiments.

Eqs. (4, 5, and 7) determine j_{xC}, j_{xA} and j_L as functions of x, if σ_A and σ_C are related to j_{xA} and j_{xC}, and proper boundary conditions are specified. On the first point, we shall assume that σ_C depends only on j_{xC}, since a simple argument shows that $j_{xC}/j_L \sim \beta h/d$, for a highly shorted generator, and similarly σ_A depends only on j_{xA}. Because the dissipation is large in the layers, they should be in the two-temperature regime, so that[7]

$$\log\sigma_C \simeq \text{const} + \alpha \log j_{xC}$$

Since α is nearly constant over quite a wide range of current density, we may write with some confidence

$$\frac{d}{dx}\left(\frac{j_{xC}}{\sigma_C}\right) = \frac{1-\alpha}{\sigma_C}\frac{dj_{xC}}{dx}; \quad \frac{\sigma_C}{\sigma_R} = \left(\frac{j_{xC}}{j_R}\right)^{\alpha} \qquad (8)$$

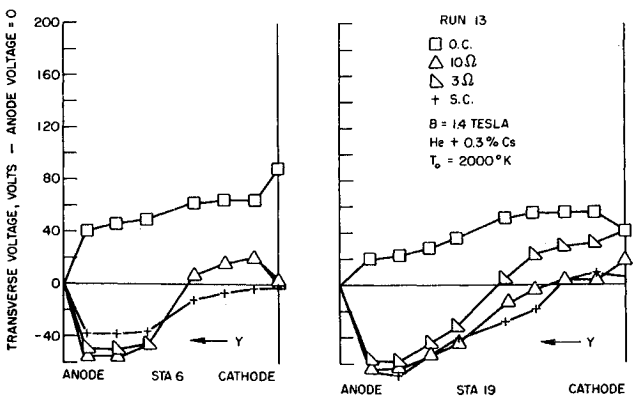

Fig. 4 Transverse voltage profiles at stations 6 and 19 for run 13, showing "reversed polarity" voltage drops for the open circuit condition.

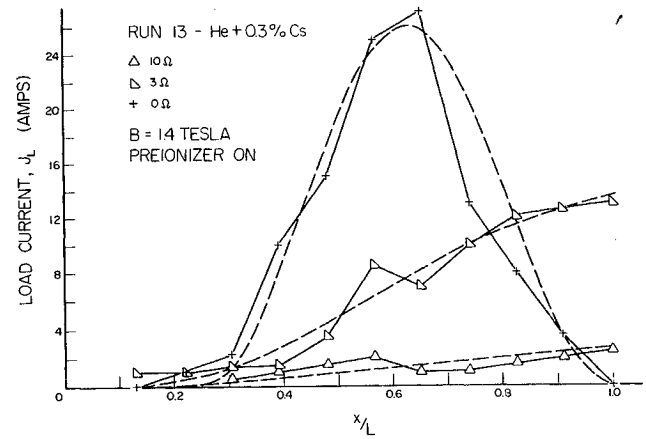

Fig. 5 Load current distributions for run 13. Dashed lines are calculated, see Sec. 5.2.

where σ_R and j_R are reference values. A similar expression can be obtained relating σ_A to j_{xA}.

4.2 Linearization and Solution

The system of differential equations is nonlinear, even with this approximation, because σ_A and σ_C in the last term of Eq. (7) depend on j_{xA} and j_{xC}. In Refs. 2 and 3 these conductivities were held constant, but this is incorrect, because in fact σ_A and σ_C vary more rapidly in x than do j_{xA}/σ_A and j_{xC}/σ_C. To obtain a consistent, if approximate, theory we shall expand Eq. (7) around a zeroth-order solution uniform in x. Thus, we put

$$j_L = \bar{j}_L + j'_L; \quad j_{xC} = \bar{j}_{xC} + j'_{xC}; \quad j_{xA} = \bar{j}_{xA} + j'_{xA}$$

$$\sigma_C = \bar{\sigma}_C + \sigma_C'; \quad \sigma_A = \bar{\sigma}_A + \sigma_A'$$

and obtain

$$\frac{d^2}{dx^2}(\rho j_L') - \beta\left(\frac{1}{\bar{\sigma}_C} - \frac{1}{\bar{\sigma}_A}\right)\frac{dj_L'}{dx} + \rho(\zeta_A^2 + \zeta_C^2) \times (j_L' + \bar{j}_L + j^*) = (1-n)\zeta_C^2\rho j^* \qquad (9a)$$

where

$$\zeta_A^2 = \frac{(\alpha-1)}{d\rho\bar{\sigma}_A} + \frac{\alpha\beta\bar{j}_L}{d\rho\bar{\sigma}_A\bar{j}_{xA}}$$

and

$$\zeta_C^2 = \frac{(\alpha-1)}{d\rho\bar{\sigma}_C} + \frac{\alpha\beta\bar{j}_L}{d\rho\bar{\sigma}_C\bar{j}_{xC}}$$

and $\bar{\sigma}_C$ is related to $\bar{j}_{xC}$ through Eq. (8), i.e., $\sigma_C'/\bar{\sigma}_C = \alpha j_{xC}'/\bar{j}_{xC}$.

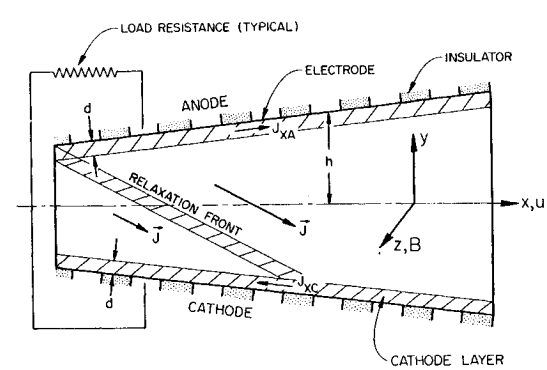

Fig. 6 Schematic of the relaxation front and current flow patterns. The front lies at an angle $\tan^{-1} t$ to the y axis and the highly conducting layers are shown along the electrode walls.

There are several parameters in this linearized perturbation equation, so that a general presentation of results is difficult. We note, however, that for conditions near short circuit, $E_{xA} \simeq E_{xC}$, so that the two layers should have nearly identical properties. Thus we take as the reference condition the symmetrical one where one half the free stream Hall current returns through each layer. This means that $\bar{j}_{xC} = \bar{j}_{xA} = \bar{j}_x$ and $\bar{\sigma}_A = \bar{\sigma}_C = \bar{\sigma}$. As a further simplification, the load resistance will be taken constant in x. This was true for all the experiments to be discussed.

For the sake of simplicity, only the case for $n = 1$ will be discussed. Hence the solutions obtained are only strictly valid for the downstream region of the generator; i.e., for $x > 2ht$. With these assumptions Eq. (9a) becomes

$$d^2(\rho j_L')/dx^2 + \rho\zeta^2(j_L' + \bar{j}_L + j^*) = 0 \tag{9b}$$

The solution for j_L' is then

$$j_L' + \bar{j}_L = A\cos\zeta x + \beta\sin\zeta x - j^* \tag{10}$$

if $\zeta^2 > 0$.

Alternatively, if $\zeta^2 < 0$, (11)

$$j_L' + \bar{j}_L = C_e^{\zeta x} + D_e^{-\zeta x} - j^* \tag{12}$$

In the special case of $\zeta L \ll 1$, which is always true at open circuit,

$$V_L' = \rho j_L' = [(1 - \alpha)/d\bar{\sigma}]j^*x^2 + Ex + F \tag{13}$$

for arbitrary $\bar{j}_{xA}$ and $\bar{j}_{xC}$. Here E and F are constants of integration.

The load currents given by Eqs. (10) and (11), and the open circuit voltage given by Eq. (13) can be compared directly with the data.

Corresponding results may be derived for the layer voltages and for the Hall field, these being the other two distinct features of the data.

The layer currents for the oscillatory solution are

$$j_{xA} = \bar{j}_{xA} - (A/d\zeta)\sin\zeta x + (B/d\zeta)\cos\zeta x \tag{14}$$

$$j_{xC} = \bar{j}_{xC} + (A/d\zeta)\sin\zeta x - B/d\zeta\cos\zeta x \tag{15}$$

The transverse layer field for the oscillatory solution is found from Eq. (6). Expanding σ, j_x and j_L and retaining zeroth and first-order terms we have

$$\bar{\sigma}(E_y - UB) = -\beta\bar{j}_x - j^* + \{A \pm B/d\zeta[\beta(1 - \alpha) + \alpha\,\bar{j}_L/\bar{j}_x]\}\cos\zeta x + \left\{B \pm \frac{A}{d\zeta}\left[\beta(1 - \alpha) + \alpha\frac{\bar{j}_L}{\bar{j}_x}\right]\right\}\sin\zeta x \tag{16}$$

where $\bar{j}_x$ and $\bar{\sigma}$, are to be read either $\bar{j}_{xC}$ and $\bar{\sigma}_C$ or $\bar{j}_{xA}$ and $\bar{\sigma}_A$, where the upper and lower signs are for the cathode and anode, respectively. Similarly, the Hall field is

$$\bar{\sigma}E_x = \bar{j}_x - \beta j^* + \left\{\beta A \pm \frac{B}{d\zeta}[(1 - \alpha) - \alpha\beta(\bar{j}_L/\bar{j}_x]\right\}\cos\zeta_x + \left\{\beta B \pm \frac{A}{d\zeta}\left[(1 - \alpha) - \alpha\beta\frac{\bar{j}_L}{\bar{j}_x}\right]\right\}\sin\zeta x \tag{17}$$

4.3 End Conditions

If we impose the end conditions on the total current, $j_L' + \bar{j}_L$, the four undetermined constants in Eqs. (10, 14, and 15), namely A, B, $\bar{j}_{xA}$ and $\bar{j}_{xC}$, may be evaluated. The current flow in the end regions is quite complex, but in essence the ends must act as resistive shunts across the generator and couple the ends of the two layers. Furthermore, the ends must redistribute the Hall current into the wall layers. We may separate those two functions of the end regions by assuming that the zeroth-order current in the wall layers is the returning Hall current and that this return mechanism does not give rise to a net voltage across the generator end. Thus

$$\bar{j}_{xA} = \bar{j}_{xC} = -\frac{h}{d}tj^*;\ \rho \neq \infty \tag{18}$$

The constants A and B are then determined by matching the load current at the ends to the perturbation currents in the wall layers. The electric field which drives the transverse current in the end region is of the order $\rho\bar{j}_L(0)/2h$. The current flowing through this region is the current flowing between the anode and cathode wall layers. The inlet end current density j_i may be obtained by assuming the axial extent of the end region to be about equal to the transverse channel dimension $2h$. Thus

$$j_{xA}'(0) = -j_{xC}'(0) = j_i(2h/d)$$

Taking the conductivity of the plasma in the inlet region to be σ_i, Ohm's law yields

$$-\rho j_L(0)\sigma_i = [j_{xA}(0) - \bar{j}_{xA}]d \tag{19}$$

Similarly in the exit region

$$-\rho j_L(L)\sigma_e = [j_{xC}(L) - \bar{j}_{xC}]d \tag{20}$$

From these conditions, we find for the oscillatory solutions,

$$\frac{A}{j^*} = \frac{s_e - s_i[s_e\sin\zeta L - \cos\zeta L]}{(s_e + s_i)\cos\zeta L + (1 - s_es_i)\sin\zeta L} \tag{21a}$$

$$\frac{B}{j^*} = \frac{s_i[s_e(\cos\zeta L - 1) + \sin\zeta L]}{(s_e + s_i)\cos\zeta L + (1 - s_es_i)\sin\zeta L} \tag{21b}$$

Here $s_e = \rho\sigma_e\zeta$ and $s_i = \rho\sigma_i\zeta$ measure the part of the total transverse current carried by the end loops. If s_e and s_i are large, the load resistance is large relative to the end region resistance and then the end loops carry a major part of the current.

For the open circuit case, continuity requires only that

$$\bar{j}_{xA} + \bar{j}_{xC} = -(2h/d)tj^* \tag{22}$$

Equation (7) may be written for the open circuit case by noting that $\rho\bar{j}_L = V_{oc}$, the load voltage, while $\bar{j}_L = 0$. Thus after linearization Eq. (7) becomes

$$dV_{oc}/dx = \frac{\bar{j}_{xC} - \bar{j}_{xA}}{\bar{\sigma}} + \frac{1 - \alpha}{\bar{\sigma}}[j_{xC}' - j_{xA}'] \tag{23}$$

But for a constant j^* current continuity requires that the current vary linearly in the wall layers. Hence we have from the integration of Eq. (4)

$$j_{xA} = j_{xA}(0) - j^*(x/d) \tag{24a}$$

and

$$j_{xC} = j_{xC}(0) + j^*(x/d) \tag{24b}$$

since the anode and cathode walls act as sink and source respectively. From the end condition we have that the current from one layer flows into the other and as in the loaded cases the returning Hall current flows symmetrically through the wall layer. Hence

$$j_{xA}(0) = j_{xC}(L) = -j_{xA}(L) = -j_{xC}(0) \tag{25a}$$

and

$$\bar{j}_{xA} = \bar{j}_{xC} \tag{25b}$$

with this assumed inlet-exit symmetry, Eq. (23) becomes

$$dV_{oc}/dx = [2(1 - \alpha)/\bar{\sigma}d]j^*(x - L/2)$$

which is readily integrated to give

$$[V_{oc}(x) - V_{oc}(0)]/UB(2h) = S(1 - \alpha)(\xi - \xi^2) \quad (26)$$

where $\xi \doteq x/L$ and

$$S = [1/UB(2h)]j^*L^2/\bar{\sigma}d$$

From the inlet end condition we find that

$$V_{oc}(0) = -(\bar{\sigma}/\sigma_i)[thd/L^2 + d/2L + (d/L)^2 \bar{j}_{xA}/j^*] \quad (27)$$

Use of the exit end condition allows us to find $\bar{j}_{xA}$:

$$\frac{\bar{j}_{xA}}{j^*} = \frac{(\bar{\sigma}/\sigma_e - \bar{\sigma}/\sigma_i)(th/2L + 1) - h\,t/d}{-\,d/2L(\bar{\sigma}/\sigma_e - \bar{\sigma}/\sigma_i) + 1} \quad (28)$$

To be strictly correct, however, we must recognize that the symmetry conditions imply that $V_{oc}(0) = V_{oc}(L)$ and hence $\sigma_e = \sigma_i$. With this condition $\bar{j}_{xA}$ becomes $\bar{j}_{xA}/j^* = \bar{j}_{xC}/j^* = -\,t\,h/d$ which is seen to be consistent with Eqs. (22) and (25).

The assumptions of this simplified model force V_{oc} to be a symmetric parabola. This is not a serious restriction, however, since the experiments indicate that the generator was so highly shorted by the end regions that $V_{oc}(0) \simeq V_{oc}(L) \simeq 0$.

The corresponding layer fields at open circuit are

$$\bar{\sigma}E_x = \bar{j}_x \pm (1 - \alpha)j^*/d(x - L/2) \quad (29)$$

where the upper and lower signs apply to the anode and cathode respectively. Furthermore

$$(E_y - uB) = -\beta E_x \quad (30)$$

from which the voltage drops in the layers may be calculated

5. Comparison with Experiments

The solutions of the linearized model will first be compared to the open circuit data, Fig. 2, and then to the loaded data, Fig. 5 of run 13.

5.1 Open Circuit Data

The best fit of Eq. (26) to the $V_{oc}(x)$ data, Fig. 2 is

$$-V_{oc}/UB(2h) \approx 0.60(\xi - \xi)^2$$

This immediately yields a value of $S(1 - \alpha) \cong 0.60$. From the definition of S we find

$$\frac{\bar{\sigma}}{\bar{\sigma}_\infty} \cong \frac{\bar{\sigma}}{r\sigma_0} = \frac{(1 - \alpha)}{0.60}\,\frac{(1 - K)}{(1 + \beta^2)}\,\frac{L^2}{2hd} \simeq \frac{96.5}{1 + \beta^2}$$

assuming $K_{oc} \simeq 0$, $d \cong 1$ cm, and $\alpha \cong 0.7$ for the layers at the high $\bar{\sigma}$. If we tentatively choose $\beta = 5$, the true microscopic value, we find $\bar{\sigma}/\bar{\sigma}_\infty = 3.7$.

We have an independent method available for estimating this conductivity ratio. First of all, we can estimate $\bar{\sigma}_\infty$, the conductivity of the core flow downstream of the relaxation region, from a simultaneous solution of Ohm's law and the two-temperature nonequilibrium model. Ohm's law for the core flow is

$$j_\infty = j_y(1 + t^2)^{1/2} \simeq UB/(1 + \beta^2)^{1/2}\,\bar{\sigma}_\infty$$

where $t \simeq \beta$ at open circuit conditions. For $\beta = 5$, this yields $j_\infty \simeq 3.7$ amp/cm^2, and from the two-temperature model we find $\bar{\sigma}_\infty \simeq 40$ mho/m at $T_e \cong 2300°$K. For $\sigma_0 = 10$ mho/m (the value of σ entering the generator) we calculate $r = 4$.

To estimate $\bar{\sigma}$ we can use the results of the open circuit model

$$\bar{j}_x = \beta\, h/d\, j_y \simeq 19 \text{ amp/cm}^2$$

From the two-temperature model for the wall layers, we find that $\bar{\sigma} = 118$ mho/m, yielding $\bar{\sigma}/\sigma_\infty \simeq 3.0$. This is in reasonable agreement with the value of 3.7 found from the best parabolic fit to the open circuit voltage, particularly considering the approximations inherent in the model.

It should be noted that smaller values of β lead to poorer agreement between the two methods. As a result, we tentatively conclude that the microscopic $\beta \simeq 5$ does represent the bulk behavior of the plasma for the open circuit data.

5.2 Loaded Data

The loaded data for run 13 consists primarily of data taken for values of $R_L = 10\ \Omega$, $3\ \Omega$ and at short circuit, all of which are very highly loaded conditions judging from the experimental result. Consequently, it seems reasonable to consider a special case of the theoretical model, valid only near short circuit, in evaluating the coefficients A and B. It appears for the aforementioned experiments that the generator was effectively shorted by the copper nozzle at the inlet making $s_i \gg 1$. In addition, estimates of exit end region resistance indicate that $s_e < 1$. For these conditions $A/j^* \approx 1$ and $B/j^* \ll 1$ near short circuit so that Eq. (10) becomes

$$j_L \approx -j^* + j^* \cos\zeta x + B \sin\zeta x \approx -\,j^*[1 - \cos(\zeta x + \Phi)]$$

where Φ is a small phase shift angle. We will adjust j^* and Φ to give a best fit to the three experimental curves (Fig. 5), and check for consistency using the electrical conductivity predictions.

At short circuit, a reasonable fit to the data is obtained for $j^* \approx -\bar{j}_L$, $\zeta L \approx 8\pi/3$ and a Φ which makes $j_L = 0$ at $\xi = 0.25$. (This fit does not force j_L to be exactly equal to zero at $\xi = 0$; there is no great loss in accuracy, however, since our model is truly valid only downstream of the relaxation front.)

It should be noted that the strong asymmetry in the short circuit load current data is attributed to the presence of an ionization front. Data from more recent runs with better preionization does show a more symmetrical load current variation at short circuit. Since better preionization should reduce the intensity of the ionization front, these data tend to support the concept of an ionization front.

We can now estimate $\bar{\sigma}$ at short circuit from

$$\bar{j}_x = \bar{j}_L\, th/d \approx -24 \text{ amp/cm}^{-2}$$

assuming $\beta \approx 5.0$. (This choice of β will be shown to be the only one which yields consistent results shortly.) From the two-temperature model, $\bar{\sigma} \approx 220$ mho/m. Putting this in the expression for ζ^2, (Eq. 9) and solving for the effective internal resistance of the electrodes we find $R_E \approx 0.3$ ohms, which is a reasonable value.

Using this value of R_E and estimating $\bar{j}_L$ for $3\ \Omega$ and $10\ \Omega$, we can calculate the resultant ζL for these load conditions from

$$\zeta L = L\,\frac{2}{\bar{\sigma}}\left\{\left[\frac{(1 - \alpha)}{(R_L + R_E)A_E d}\right]\left[\frac{\alpha}{1 - \alpha}\,\frac{\beta d}{th} - 1\right]\right\}^{1/2}$$

These are tabulated in Table 3 for $\alpha = 0.80$, $\beta \approx 5$ and $t = 3.0$. From the plotted values in Fig. 5, we see that these constitute a good first order fit to the data for all three load conditions.

Table 3 Generator parameters at loaded operation

$R_L + R_E$, ohm	$A' \approx \bar{J}_L$, amp	$\bar{j}_{xw}$, amp/cm^{-2}	$\bar{\sigma}_w$, mho/m^{-1}	ζL	$(\xi)_{j_L} = 0$
$0 + 0.3^a$	13^a	24.0	220	$2.67\pi^a$	0.25^a
$3 + 0.3$	7^a	13	140	1.0π	0.10^a
$10 + 0.3$	1.5^a	2.8	48	0.90π	0.10^a

[a] Values selected to match experimental data.

As a further check on the consistency of our results we calculate σ_∞ by two independent methods. From the two-temperature model we find $\bar{\sigma}_\infty \approx 45$ mho/m using

$$j_\infty = j_y(1 + t^2)^{1/2} \approx 4.5 \text{ amp/cm}^{-2}$$

for $\beta = 5.0$ and $t = 3.0$. From Ohm's law

$$\bar{\sigma}_\infty \approx \frac{j_y(1 + \beta^2)}{UB(1 - K)(1 + \beta\beta_{app})} \approx 44 \text{ mho/m}$$

using the experimental values of $K \approx 0.1$, $\beta_{app} \approx 0.2$, and assuming $\beta \approx 5.0$. This good agreement is only achieved for $\beta \approx 5.0$ and hence serves essentially to verify the choice of the effective value of β. Assuming $\sigma_0 \approx 10$ mho/m as before we find $r \approx 4.5$.

As a final check, we can estimate the average axial electric field at short circuit

$$\bar{E}_{xC} \approx \frac{\bar{j}_L}{\bar{\sigma}} \beta \left[\frac{th}{\beta d} + 1 \right] \approx -14.6 \text{ v/cm}$$

again using $\beta \approx 5.0$. The experimental value is approximately -10 v/cm, which is reasonable agreement.

The predicted values of the transverse layer voltages are in poor agreement with the experimental results. However, it may be that this comparison is confused by the relaxation front impinging on the cathode wall and by a possible separation along the anode wall.

The theory of nonuniformities and ionization instabilities is not sufficiently complete to be able to verify that an effective Hall parameter of about 5 is correct. (The theory for plane electrothermal waves predicts a value of $\beta_{eff} \approx 0.6$ for helium plus 0.3% cesium.) Thus for the moment we must consider our choice of $\beta \approx 5.0$ as a best guess.

5.3 Relation to other Experiments

To the authors' knowledge, the severe layer shorting phenomena described here have not been prominent in the other large scale linear generator experiments reported to date. One of these experiments[8] operates at subsonic velocities, with a much smaller ratio of electron to gas temperatures than in the present experiment. The subsonic flow also results in a ratio of densities in the electrode boundary layer and free-stream which is near or above unity, whereas this ratio is smaller in the supersonic channel. Both of these factors lessen the tendency to electrode-wall breakdown in the subsonic channel.

A second large segmented generator has been operated supersonically, with mixtures of noble gases,[9] and in a shock tunnel. This generator has performed quite well for the very short (millisecond) test times available with the shock tunnel, with no clear evidence of layer shorting. It does, however, exhibit electrode drops which are as large as half the open circuit voltage. These are much larger than the electrode drops in the present experiment, and seem to suggest the existence of a high resistance layer on the electrode wall. Such a layer would impede the type of shorting we have found.

6. Summary and Conclusions

The proposed model of a nonequilibrium MHD generator yields predictions which agree with many of the prominent features of the experimental results. In particular, 1) The model predicts the observed parabolic shape for the open circuit voltage when strong end-loop shorting is present. 2) Using a best fit to the experimental V_{oc} data, a consistent set of average values for the layer and free stream conductivities is obtained. For $\sigma_0 \approx 10$ mho/m at the entrance to the generator, we find that $\bar{\sigma}_\infty \approx 40$ mho/m after the relaxation front and $\bar{\sigma} \approx 120$ mho/m in the wall layers. Direct measurements of the electron density are required to verify these predictions.

3) The consistent results just quoted are obtained only for a Hall parameter, $\beta \approx 5$, close to the true microscopic value.

4) Near short circuit a perturbation solution yields oscillatory solutions which agree qualitatively with the observed axial variation of the load current. In particular, the slow buildup of the load current is probably due to the low maximum axial electric field of about 10 v/cm the helium plus 0.3% cesium mixture can withstand before breaking down (i.e., going into the strongly nonequilibrium conduction mode), along the electrode wall.

5) Fitting the theoretical curves to the data again yields a consistent set of electrical conductivity values for $\beta \approx 5$. At short circuit we find that for $\sigma_0 \approx 10$ mho/m, $\sigma_\infty \approx 45$ mho/m and $\bar{\sigma} \approx 220$ mho/m.

6) The values of conductivities mentioned differ from the open circuit case, only in the value of $\bar{\sigma}$. The values of the Hall parameter which yielded these results was $\beta \approx 5$ in both cases. The difference may be due to the somewhat larger Hall field attained in the loaded condition, due to the load currents being drawn through the electrode wall layers.

References

[1] Kerrebrock, J. L. et al., "A Large Nonequilibrium MHD Generator," *Proceedings of the Symposium-Electricity from MHD*, SM-74/163, Vol. 2, Salzburg, Austria, July 1966.

[2] Decher, R., "Experimental Investigation of a Nonequilibrium Magnetohydrodynamic Generator," Ph.D. thesis, Feb. 1968, M.I.T., Cambridge, Mass.

[3] Decher, R. and Kerrebrock, J. L., "Electrode Wall End-Loop Shorting in a Nonequilibrium Generator," *9th Symposium on Engineering Aspects of MHD*, Tullahoma, Tenn., April 1968.

[4] Kerrebrock, J. L., "Segmented Electrode Losses in MHD Generators with Nonequilibrium Ionization," *AIAA Journal*, Vol. 4, No. 11, Nov. 1966, pp. 1938–1947.

[5] Hoffman, M. A., "Simplified Model of Segmented Electrode Losses in Nonequilibrium MHD Generators," M.I.T. CSR TR-66-7, Aug., 1966, Cambridge, Mass.

[6] Kerrebrock, J. L. and Hoffman, M. A., "The MIT nonequilibrium MHD generator," SM-107/25, 1968, *Electricity from MHD*, IAEA, Vienna, Austria.

[7] Kerrebrock, J. L., "Nonequilibrium Ionization Due to Electron Heating: I. Theory," *AIAA Journal*, Vol. 2, Nov. 1964, pp. 1072–1080.

[8] Bertolini et al., "Subsonic constant-area MHD generator experiments with the CNEN blow-down loop facility," SM-107-197, 1968, *Electricity from MHD*, IAEA, Vienna, Austria.

[9] Zauderer, B. and Tate, E., "Performance of a large scale, nonequilibrium MHD generator with rare gases, Part II," *Eleventh Symposium on Engineering Aspects of MHD*, March 24–26, 1970, California Institute of Technology, Pasadena, Calif.